Article

Microfluidic chain reaction of structurally programmed capillary flow events

Mohamed Yafia[1,2,4], Oriol Ymbern[1,2,4], Ayokunle O. Olanrewaju[1,2,3], Azim Parandakh[1,2], Ahmad Sohrabi Kashani[1,2], Johan Renault[1,2], Zijie Jin[1,2], Geunyong Kim[1,2], Andy Ng[1,2] & David Juncker[1,2 ✉]

Chain reactions, characterized by initiation, propagation and termination, are stochastic at microscopic scales and underlie vital chemical (for example, combustion engines), nuclear and biotechnological (for example, polymerase chain reaction) applications[1–5]. At macroscopic scales, chain reactions are deterministic and limited to applications for entertainment and art such as falling dominoes and Rube Goldberg machines. On the other hand, the microfluidic lab-on-a-chip (also called a micro-total analysis system)[6,7] was visualized as an integrated chip, akin to microelectronic integrated circuits, yet in practice remains dependent on cumbersome peripherals, connections and a computer for automation[8–11]. Capillary microfluidics integrate energy supply and flow control onto a single chip by using capillary phenomena, but programmability remains rudimentary with at most a handful (eight) operations possible[12–19]. Here we introduce the microfluidic chain reaction (MCR) as the conditional, structurally programmed propagation of capillary flow events. Monolithic chips integrating a MCR are three-dimensionally printed, and powered by the free energy of a paper pump, autonomously execute liquid handling algorithms step-by-step. With MCR, we automated (1) the sequential release of 300 aliquots across chained, interconnected chips, (2) a protocol for severe acute respiratory syndrome-coronavirus-2 (SARS-CoV-2) antibodies detection in saliva and (3) a thrombin generation assay by continuous subsampling and analysis of coagulation-activated plasma with parallel operations including timers, iterative cycles of synchronous flow and stop-flow operations. MCRs are untethered from and unencumbered by peripherals, encode programs structurally in situ and can form a frugal, versatile, bona fide lab-on-a-chip with wide-ranging applications in liquid handling and point-of-care diagnostics.

The MCR encodes the deterministic release of reagents stored in a series of reservoirs, with the release of reservoir n being conditional on the emptying (draining) of the reagent in reservoir $n-1$, and emptying reservoir n, in turn triggering the release of reservoir $n+1$. Capillary domino valves (CDVs) encode this condition, and serially connect, that is, chain, the reservoirs, and thus control the propagation of the chain reaction (Fig. 1a). MCRs were implemented in three-dimensionally printed circuits made with a common stereolithography printer with feature size from 100 μm to 1.5 mm, hydrophilized using a plasma chamber (Extended Data Fig. 1 and 2), sealed with a plain cover and connected to a capillary pump made of paper (filter papers or absorbent pads). The paper was spontaneously wetted by aqueous solution drawn from the microfluidic circuit by releasing free energy stored in the paper surface, and this drove the chain reaction; expressed differently, the capillary pump generated a negative capillary pressure that was hydraulically transmitted back into the circuit through the main channel and serially drained side-reservoirs connected by a small conduit, called the

functional connection (further described below). CDVs form air links between adjacent reservoirs, serially connecting them along a path parallel to the main channel, but interrupted by filled reservoirs that form liquid plugs between CDV air links. When the (first) reservoir connected to the air vent through a continuous air link is emptied, the plug is removed and the length of the air link propagates to the next filled reservoir in the MCR (Fig. 1a–d and Supplementary Video 1). This simple design structurally encodes the conditional propagation of capillary flow events and the step-by-step release of an arbitrary number N of reservoirs without peripheral connections or moving parts, and is further detailed in the Supplementary Information.

MCRs require ancillary capillary microfluidic components that fulfil different functions depending on the intended operation (for example, loading, holding, mixing and draining liquids following the MCR progression) to form fully integrated and scalable capillaric circuits (CCs). CCs are designed on the basis of a library of building blocks including capillary pumps, flow resistances and many types of capillary
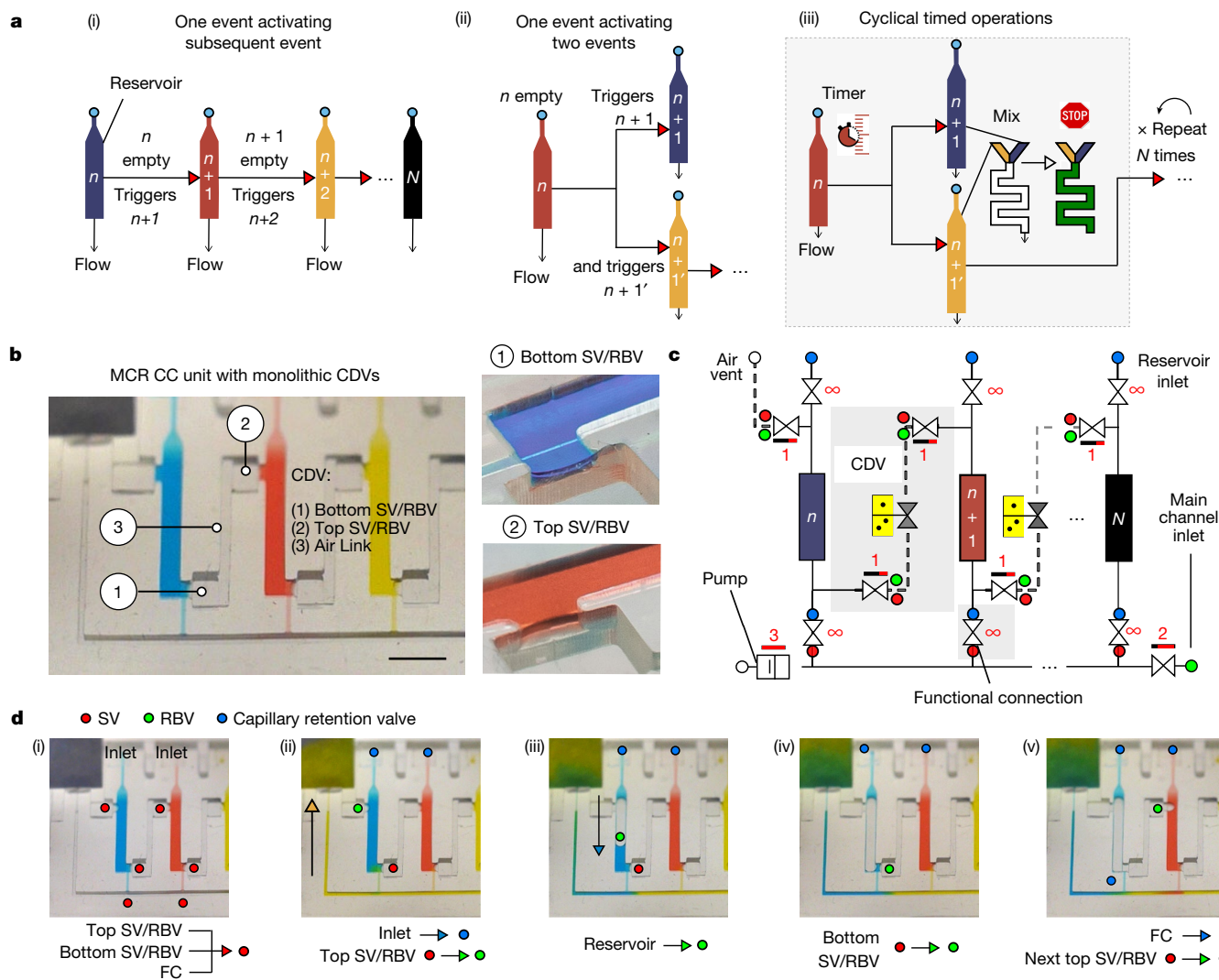
Fig. 1 | MCR with monolithic CDV for serial delivery of reagents in capillaric circuits (CCs). a, (i) Serial MCR, (ii) branching MCR, (iii) cascaded, timed MCR. **b**, MCR unit with three reservoirs chained through CDVs and close-up of dual function SV/RBVs that keep liquid out of the CDV air link (forming a pneumatic connection) and prevent premature drainage. **c**, Symbolic view of the MCR unit with capillary retention valves (infinity symbol), CDV (grey overlay) that includes an air link, two SV/RBVs and functional connection. **d**, Screen shots of Supplementary Video 1 showing MCR sequences in which most of the capillary elements have dual functions, one during reagent loading, one during MCR

propagation. (i) A loaded chip with liquids confined to the reservoirs by physical and capillary valves. (ii) MCR is triggered (the inlet becomes a capillary retention valve and the top SV becomes a RBV). (iii) Emptying of the first reservoir on bursting of the top RBV. (iv) The bottom SV momentarily becomes an RBV that bursts immediately. (v) Air now occupies the emptied reservoir. The functional connection (FC) becomes a capillary retention valve preventing the air from penetrating into in the main channel. The air link connects the air to the RBV of the next reservoir, which bursts and triggers reservoir emptying. Scale bar, 2 mm.

valve (stop valves (SVs), trigger valves, retention valves, retention burst valves (RBVs))[12,14], and thus are analogous to microelectronic integrated circuits, but lacking the scalability and functionality. In MCRs, samples are loaded by capillary flow through an inlet with a capillary retention valve and entirely fill the reservoirs lined with three SVs, including two with a dual RBV function connecting to the two lateral CDVs, and one at the intersection of the functional connection and the main channel (Fig. 1c). Although the functional connection is a deceptively simple straight channel, it fulfils six key functions. It is (1) the air vent during filling of the reservoir, and (2) a SV preventing the reagent from spilling into the main channel while it is empty. After filling of the main channel, it forms a (3) hydraulic link propagating the pressure from the main channel into the reservoir and (4) a barrier (and bottleneck) to the diffusion of reagents between the reservoir and the main channel. (5) It becomes the outlet and a flow resistance (discussed further below) during reservoir emptying, and (6) a capillary retention valve stopping

air from invading the main conduit after the reservoir is emptied. As a result, many trade-offs guide its design.

We sought to understand the design window and failure modes of MCRs, notably under which conditions downstream of CDVs might trigger prematurely, using both theory and experiments. MCR-CCs incorporate numerous capillary SVs according to previously established design criteria[13] and while considering three-dimensional (3D) printer performance including resolution, imprecision and printing errors. We then analysed the MCR based on an electrical circuit analogy (Extended Data Fig. 3) and derived a simplified circuit that neglects minor resistances (Fig. 2a)[13]. Successful and incremental propagation of the MCR is conditional on preventing the breach of the liquid in reservoir n into the CDV and air link connecting $n + 1$, which is equivalent to stating that all the liquid in reservoir n must flow exclusively through the functional connection n.

The flow path from reservoir n to $n + 1$ is interrupted by the CDV, which includes the capillary SV at one extremity and RBV at the other, with

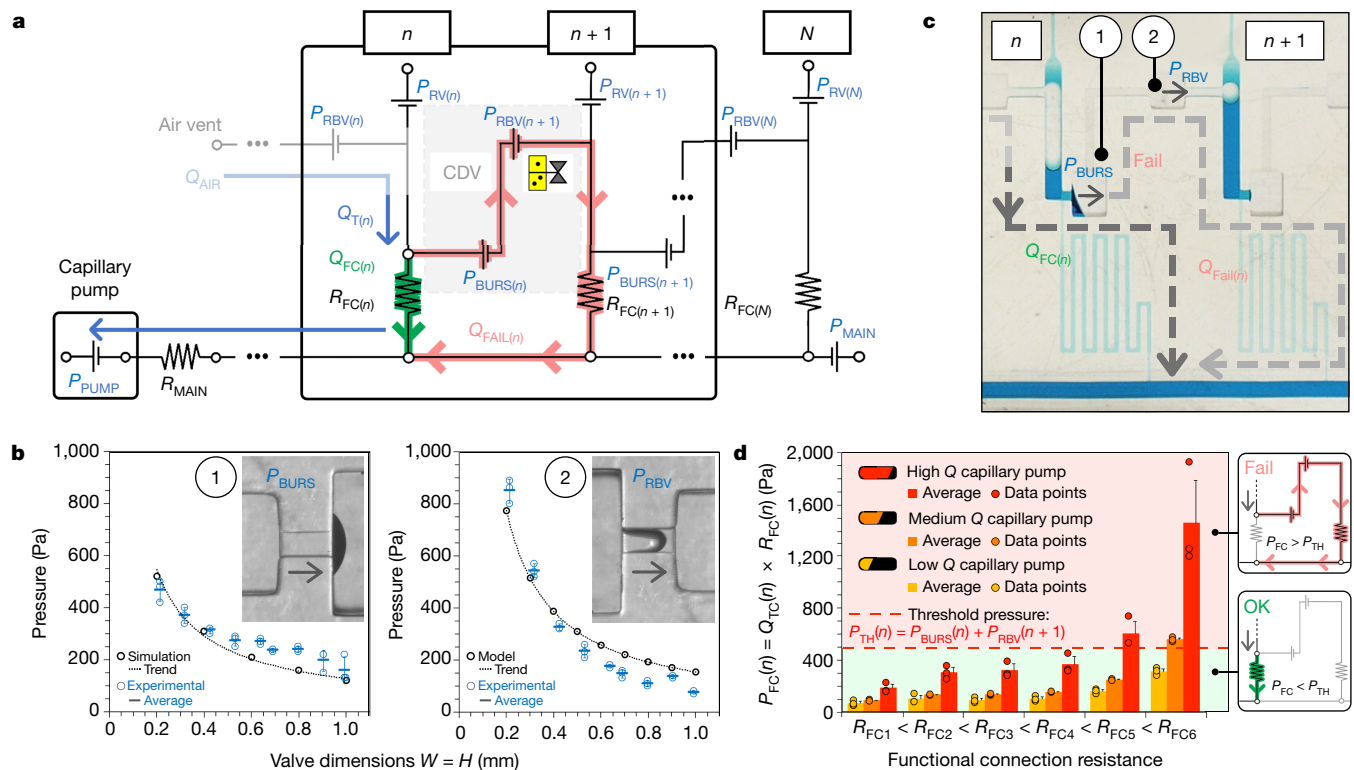**Fig. 2 | Circuit analysis and experiments identify operational window for MCRs. a**, The simplified equivalent electrical circuit of the MCR units shown in Fig. 1. **b**, Experimental SV burst pressure (1) and RBV retention pressure (2) for valves with conduits with different, square cross-sections fitted with a numerical and an analytical model, respectively. **c**, Illustration of failure for a CDV with long serpentine FCs with very high resistance leading to liquid breach inside the air link, and premature draining of reservoir $n+1$. **d**, Tests of six MCRs

with increasing R_{FC} and three different paper pumps to determine the effect of varying the flow rate ($n=3$ for each paper pump and R_{FC}). All data points are shown in **b** and **d**. Error bars are standard deviations from three experiments, the centre of each error bar is the mean value. As predicted, the CDVs fail when the pressure drop across the FC $P_{FC(n)}$ exceeds the CDV threshold pressure $P_{BURS(n)} + P_{RBV(n+1)}$.

bursting thresholds of P_{BURS} and P_{RBV}, respectively. If either of these valves fails prematurely, then the propagation of the MCR is at risk of disruption. But because both valves are pneumatically connected by the air trapped within the air link, their pressures are additive and hence the threshold for failure of either is the sum of the two. The condition for success is $Q_{FAIL} = 0$, which during drainage of reservoir n is satisfied if the pressure drop on the functional connection (FC) $P_{FC} = Q_{FC} \times R_{FC}$ is (see also Supplementary Information for a detailed mathematical derivation):

$$P_{FC(n)} < P_{BURS(n)} + P_{RBV(n+1)} \qquad (1)$$

We calculated P_{BURS} (numerically)[20] and P_{RBV} (analytically, Supplementary Information) for conduits with a square cross-section ($W = H$) for the typical dimension in our 3D-printed CCs, and measured them experimentally for validation (Fig. 2b and Extended Data Fig. 4). Both P_{BURS} and P_{RBV} are inversely proportional to the smallest dimension of the rectangular conduit. We accounted for the hydrophobic ceiling formed by the sealing tape in both cases (Extended Data Fig. 2b), and which is a key feature to forming a functional SV[20]. Note that because of the comparatively low pressures and small volume of the air links, the compressibility of air is negligible here.

Next, several MCRs featuring functional connections with large and increasing R_{FC} were tested with pumps with different capillary pressure and flow rates. The interplay between the resistance and the flow rate determines the operational window for the CDV while they are inversely proportional. We found excellent concordance between theory and experiments for the operation window of the MCR, and failure only occurred for the highest values of R_{FC} (nos. 5 and 6), and for only the

most powerful capillary pumps (Fig. 2c,d and Extended Data Fig. 5). The MCR designs used in the proof-of-concept applications, shown below, are well within the failure threshold, helping to ensure reliable propagation of the chain reaction.

We designed a chip-to-chip interface with a leakage-free connection for liquid (main channel) and air (connecting the CDVs), respectively, and connected four chips with 75 MCRs each (Fig. 3a and Supplementary Video 2). This result illustrates the reliability of the MCR and of CDVs, and demonstrates integrated, large-scale fluidic operations by 'passive' capillary microfluidics, beyond the capability of many 'active', computer programmable microfluidic systems.

Automated SARS-CoV-2-specific saliva antibody detection assay

We measured antibodies against the nucleocapsid protein (N protein) of SARS-CoV-2 in saliva, with application potential for early infection detection[21,22], initial patient assessment as prognosis indicator[23] and for serosurveys to differentiate vaccinated and naturally infected individuals[24]. Conventional lateral flow assays with predried reagents are simple to operate, but typically do not include enzymatic amplification that underlies the laboratory enzyme-linked immunosorbent assay (ELISA), and have to be read out within a few minutes of completion. Here, we used MCR to automate a sequence of eight steps in common laboratory ELISA protocols (Fig. 3b and Supplementary Video 3). The chip is connected to a small paper pump to drain excess buffer, and a nitrocellulose strip for assay readout itself connected to a large-capacity paper pump that drives the MCR. Note that the MCR propagates in a
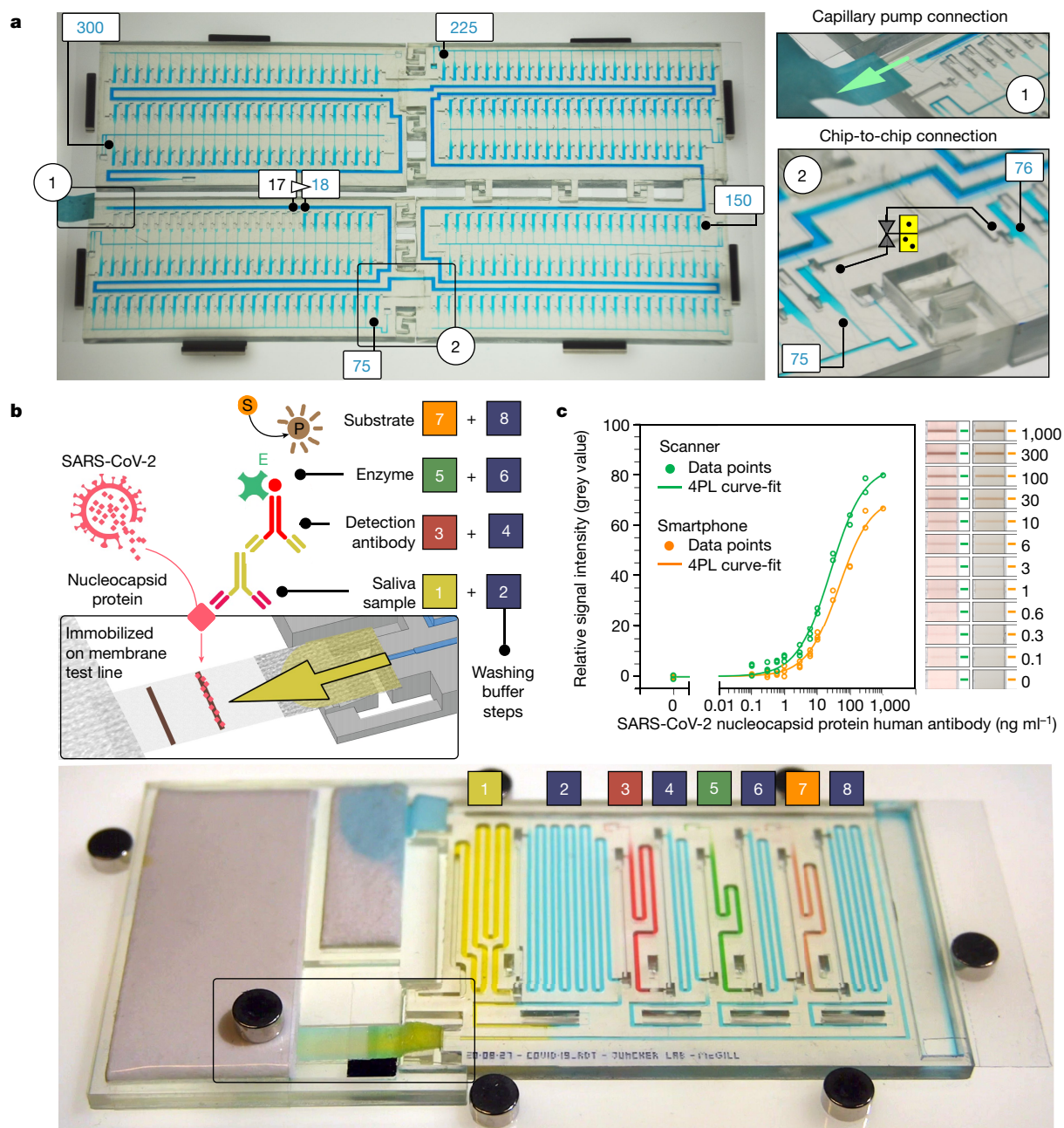
Fig. 3 | Large-scale MCR and COVID-19 serology assay in saliva. a, A MCR of 300 aliquots stored in 4.9 µl reservoirs across four chained and interconnected chips (Supplementary Video 2). **b**, SARS-CoV-2 antibody detection in saliva. Sequential, preprogrammed release of reagents by MCR is triggered by connecting the paper pump (Supplementary Video 3). The MCR supplies four reagents and four buffers in sequence. The functionality includes delivery and removal (by flushing) of solutions, metering (40–200 µl) by reservoir size, flow speed and time control by the flow resistance of the FC and the capillary pressure of the paper pump. The enzymatic amplification produces a brown precipitate line visible to the naked eye. **c**, Assay results and binding curve obtained by spiking antibody into saliva, and imaging by scanner and cell phone with representative images of the detection zone for each concentration, indicating the potential for quantitative point-of-care assays. **d**, An assembled chip filled with coloured solutions highlighting the channels for the different reagents and washing buffer.

direction opposite from the flow in the main channel, and reagents released sequentially from reservoirs all flow past previously emptied reservoirs, thus minimizing the diffusional mixing between reagents. We used 3,3'-diaminobenzidine as a substrate that on enzymatic conversion produced a brown, persisting precipitate that could serve both as an immediate readout and a record for archival. Assay parameters such as volume, time and reagent concentrations were optimized extensively following standard protocols (see Extended Data Fig. 6 for examples) and will be reported elsewhere. The result can be visualized by the naked eye

or quantified using a scanner or a smartphone integrated with a simple folded origami box to minimize light interference, with a sensitive, quantitative and reproducible output (Fig. 3c and Extended Data Figs. 7 and 8).

Automated microfluidic thrombin generation assay (TGA)

Routine coagulation tests (prothrombin time and activated partial thromboplastin time) are used as initial evaluation of haemostatic
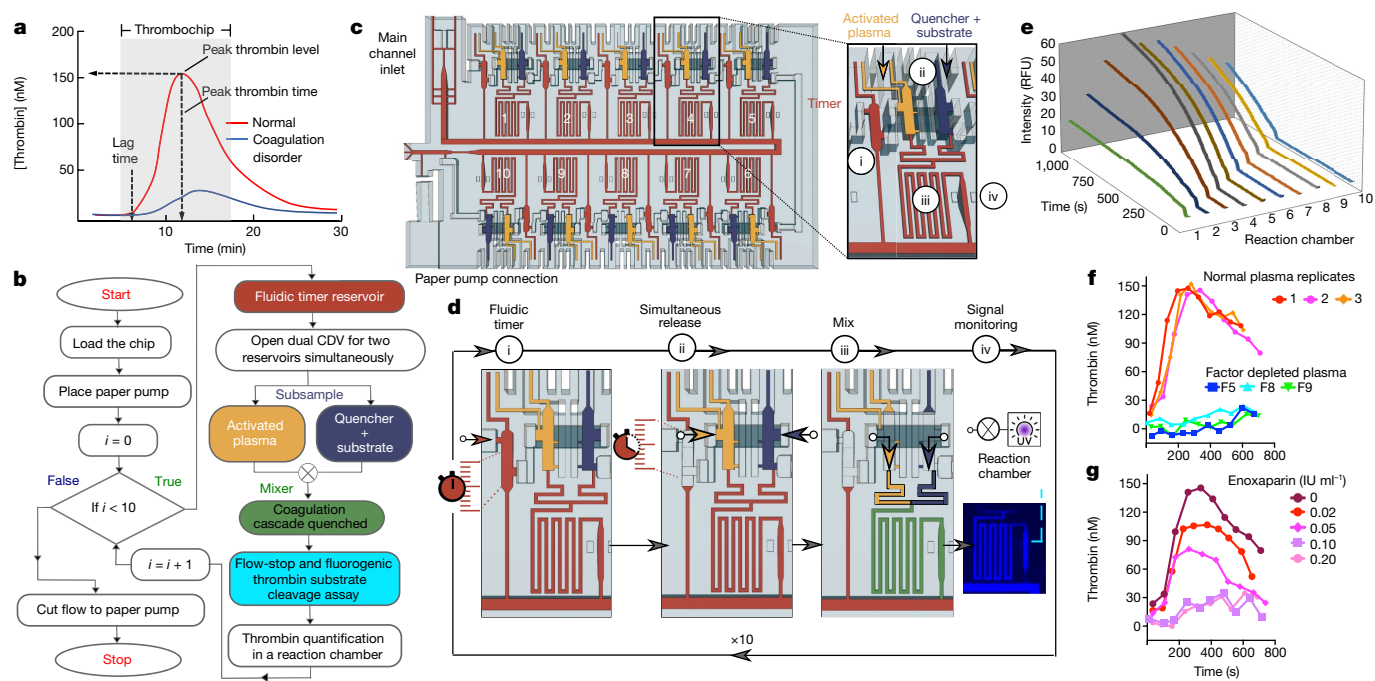
Fig. 4 | Automated TGA by continuous analysis of plasma subsamples (thrombochip). a, Model thrombin generation curve (thrombograms) for plasma with normal (red) and disordered (blue) coagulation. The grey box is the time window of the thrombochip. **b**, TGA operations and algorithm encoded in the thrombochip. **c**, Schematic of the thrombochip with inset. **d**, The (i) timer, (ii) simultaneous release of defibrinated plasma and reagents (quencher and substrate), (iii) mixing and (iv) flow-stop in the reaction chamber and monitoring of the fluorescence time-course signal. **e**, Fluorescent thrombin substrate turnover in the ten 1-min interval subsamples; the slope of each curve is proportional to thrombin concentration, and is one data point in the thrombogram. **f**, **g**, Abridged thrombograms of defibrinated human plasma that is normal (three replicates of pooled plasma), factor depleted (F5, F8, F9; single measurement for each factor) (**f**) and mixed with anticoagulant drug (Enoxaparin) at different concentrations (**g**) (single measurement at each concentration). The thrombin generation time-courses are concordant with expectations.

status. These tests terminate on clot formation and thus only inform on the initiation of clotting, whereas the coagulation cascade continues and generates 95% of total thrombin (the final enzyme in the coagulation cascade)[25]. The haemostatic capacity, expressed as the endogenous thrombin potential, can therefore not be fully evaluated by these tests[26]. Global coagulation assays, such as the TGA that provides the time-course of active thrombin concentration in clotting plasma, are better measures of haemostatic function. Peak height, shape and area under curve of the thrombin generation curve (also known as the thrombogram, Fig. 4a) can be determined and correlated to clinical phenotypes to investigate coagulation disorders, and measure the effect of anticoagulants[27]. The first TGA was introduced in the 1950s, and involves the activation of coagulation of blood or plasma, followed by a two-stage assay that requires the collection and mixing of subsamples with fibrinogen (or chromogenic substrates following their availability) at precisely timed intervals (for example, 1 min) over the course of 20 min or so, followed by the quantification of thrombin in each of them[28,29]. The labour intensity, strict timing requirements and risk of error are great obstacles to wider adoption and clinical use of TGAs-by-subsampling. The calibrated automated thrombogram (CAT) introduced in 2002 simplifies operations thanks to newly synthesized thrombin substrates, a calibration TGA using the patient sample spiked with reference material and mathematical extrapolation[30].

Here, we demonstrate the capacity of MCR to automate the original TGA-by-subsampling in a microfluidic implementation that we called a "thrombochip". We devised an algorithm (Fig. 4b) for automating and timing the procedure with cascaded, iterative and branching fluidic operations, and structurally programmed it into a 3D-printed chip (Fig. 4c, Extended Data Fig. 9 and Supplementary

Video 4). Defibrinated, coagulation-activated plasma subsamples and reagent were loaded into the thrombochip, and on triggering of the MCR, without further intervention, they were released at 1 min intervals from the ten pairs of reservoirs, mixed in the serpentine mixer and stored in a 2.1 µl reaction chamber with a width of 500 µm for fluorescence signal generation and readout using a camera (Supplementary Videos 5 and 6). The concentration of thrombin in each of the subsamples is proportional to the rate of the fluorescent substrate turnover, and the time-course of thrombin is reported as a thrombogram.

Reliable execution of the TGA subsample analysis algorithm faced several practical challenges, and in particular draining of two reservoirs simultaneously is inherently unstable. Indeed, as soon as one reservoir starts being drained, the (absolute) pressure in the CC drops, and readily falls below the threshold of the RBV of the second reservoir, which will not burst, meaning the reservoir will remain filled. The MCR and 3D printing helped overcome this challenge and the reservoir pair containing plasma and reagents could be drained synchronously. An embedded air link connecting the outlet of reservoir n to the RBVs of both $n + 1$ and $n + 1'$, which were identical and very weak RBVs (cross-section, 1×1 mm²) lead to simultaneous bursting and reliable propagation of the chain reaction. Other critical features are a serpentine mixer; stop-flow and holding of the solution in the reaction chambers for the thrombin quantification; a pressure pinning structure at the main outlet to cut the hydraulic connection to the paper pump after completion of the fluidic operation; an RBV at the main outlet that pins liquid and helps prevent backflow to safeguards the reaction chambers from uncontrolled mixing and finally evaporation during the extended monitoring and imaging of the thrombin reaction.

As validation of the thrombochip, human pooled plasma, plasma depleted of Factors V, VIII and IX, and plasma spiked with the anticoagulant Enoxaparin (an anti-Factor Xa drug) were analysed. The corresponding thrombograms were reproducible, consistent with normal and impaired coagulation cascades caused by factor depletion, and measured the dose-response of Enoxaparin (Fig. 4f, g). The general profile of the thrombograms generated in these proof-of-concept experiments are comparable to those by CAT and other microtitre plate-based assays[31,32], but direct comparison of the data such as lag time and peak concentration requires standardized sample processing, reference materials and normalization, which can guide future development of the thrombochip.

Conclusion and discussion

MCRs introduce deterministic, modular and programmable chain reactions at the mesoscale and constitute a new concept for autonomous, programmable liquid operations and algorithms by control of both hydraulic and pneumatic flow and connectivity. The automation of complex and repetitive liquid handling operations has so far only been possible with a computer, software programs and cumbersome peripheral equipment, either robotics or, in the case of microfluidics[6], systems to supply reagents, power or flow control[8–11]. MCR introduces mesoscale chain reactions as a frugal, integrated, scalable and programmable process that power integrated labs-on-a-chip.

The MCR chip micro-architecture is simultaneously the circuit and the code of the chain reaction, is manufacturable with a variety of techniques and scalable along two distinctive paths: First, following microelectronics example and Moore's law, by shrinking and increasing the number of features per unit area and per unit volume (for example, by using 3D printing). Second, by expanding the overall size of CC-MCRs by interconnecting and chaining chips, and, inspired by trees that draw liquids more than 100 m in height, linking them to powerful capillary pumps[33]. We anticipate numbers of steps far beyond the 300 shown here, and far more complex algorithms than the ones of the thrombochip.

MCRs are generalizable, compatible with positive pressure operations and could be interfaced with active microfluidics and robotic liquid handling systems. Spontaneous, capillary flow MCRs may be further improved too with permanently hydrophilic resins or coatings, liquid storage pouches and predried reagents[34], notably for point-of-care applications and any other uses. An end-user, by simply depositing a drop of solution at the inlet, could trigger a choreography of timed operations including aliquoting, delivery, mixing, flushing and reactions of several chemicals. As MCRs can be 3D-printed and monolithically encoded in a chip, the entry barrier is very low (entry-level resin-based printers cost <US$300). MCRs may be home-manufactured easily, or mail-ordered, opening the way for rapid dissemination and for new inventions, advances and for downloadable and printable microfluidic apps.

Online content

Any methods, additional references, Nature Research reporting summaries, source data, extended data, supplementary information, acknowledgements, peer review information; details of author contributions and competing interests; and statements of data and code availability are available at https://doi.org/10.1038/s41586-022-04683-4.

1. Denisov, E., Sarkisov, O. & Likhtenshtein, G. I. *Chemical Kinetics: Fundamentals and Recent Developments* (Elsevier, 2003).
2. *Award Ceremony Speech*. Nobel Media AB 2021 (Nobel Prize Organization, 2021); https://www.nobelprize.org/prizes/chemistry/1956/ceremony-speech/
3. Mullis, K. et al. Specific enzymatic amplification of DNA in vitro: the polymerase chain reaction. *Cold Spring Harb. Symp. Quant. Biol.* **51**, 263–273 (1986).
4. Saiki, R. K. et al. Primer-directed enzymatic amplification of DNA with a thermostable DNA polymerase. *Science* **239**, 487–491 (1988).
5. Dirks, R. M. & Pierce, N. A. Triggered amplification by hybridization chain reaction. *Proc. Natl Acad. Sci. USA* **101**, 15275–15278 (2004).
6. Sackmann, E. K., Fulton, A. L. & Beebe, D. J. The present and future role of microfluidics in biomedical research. *Nature* **507**, 181–189 (2014).
7. Manz, A., Graber, N. & Widmer, H. M. Miniaturized total chemical analysis systems: a novel concept for chemical sensing. *Sens. Actuators B. Chem.* **1**, 244–248 (1990).
8. Thorsen, T., Maerkl, S. J. & Quake, S. R. Microfluidic large-scale integration. *Science* **298**, 580–584 (2002).
9. Choi, K., Ng, A. H., Fobel, R. & Wheeler, A. R. Digital microfluidics. *Annu. Rev. Anal. Chem.* **5**, 413–440 (2012).
10. Strohmeier, O. et al. Centrifugal microfluidic platforms: advanced unit operations and applications. *Chem. Soc. Rev.* **44**, 6187–6229 (2015).
11. Easley, C. J. et al. A fully integrated microfluidic genetic analysis system with sample-in-answer-out capability. *Proc. Natl Acad. Sci. USA* **103**, 19272–19277 (2006).
12. Olanrewaju, A., Beaugrand, M., Yafia, M. & Juncker, D. Capillary microfluidics in microchannels: from microfluidic networks to capillary circuits. *Lab Chip* **18**, 2323–2347 (2018).
13. Olanrewaju, A. O., Robillard, A., Dagher, M. & Juncker, D. Autonomous microfluidic capillaric circuits replicated from 3D-printed molds. *Lab Chip* **16**, 3804–3814 (2016).
14. Safavieh, R. & Juncker, D. Capillarics: pre-programmed, self-powered microfluidic circuits built from capillary elements. *Lab Chip* **13**, 4180–4189 (2013).
15. Ozer, T., McMahon, C. & Henry, C. S. Advances in paper-based analytical devices. *Annu. Rev. Anal. Chem.* **13**, 85–109 (2020).
16. Wang, X., Hagen, J. A. & Papautsky, I. Paper pump for passive and programmable transport. *Biomicrofluidics* **7**, 14107 (2013).
17. Kokalj, T., Park, Y., Vencelj, M., Jenko, M. & Lee, L. P. Self-powered imbibing microfluidic pump by liquid encapsulation: SIMPLE. *Lab Chip* **14**, 4329–4333 (2014).
18. Dal Dosso, F. et al. Creasensor: SIMPLE technology for creatinine detection in plasma. *Anal. Chim. Acta* **1000**, 191–198 (2018).
19. Achille, C. et al. 3D printing of monolithic capillarity-driven microfluidic devices for diagnostics. *Adv. Mater.* **33**, e2008712 (2021).
20. Glière, A. & Delattre, C. Modeling and fabrication of capillary stop valves for planar microfluidic systems. *Sens. Actuator A Phys.* **130-131**, 601–608 (2006).
21. Burbelo, P. D. et al. Sensitivity in detection of antibodies to nucleocapsid and spike proteins of severe acute respiratory syndrome coronavirus 2 in patients with coronavirus disease 2019. *J Infect. Dis.* **222**, 206–213 (2020).
22. Pisanic, N. et al. COVID-19 serology at population scale: SARS-CoV-2-specific antibody responses in saliva. *J. Clin. Microbiol.* **59**, e02204–e02220 (2020).
23. Batra, M. et al. Role of IgG against N-protein of SARS-CoV2 in COVID19 clinical outcomes. *Sci Rep.* **11**, 3455 (2021).
24. Beck, E. J. et al. Differentiation of Individuals Previously Infected with and Vaccinated for SARS-CoV-2 in an Inner-City Emergency Department. *J. Clin. Microbiol.* **60**, e02390–e02421 (2022).
25. Tripodi, A. Thrombin generation assay and its application in the clinical laboratory. *Clin. Chem.* **62**, 699–707 (2016).
26. Brummel-Ziedins, K. E. & Wolberg, A. S. Global assays of hemostasis. *Curr. Opin. Hematol.* **21**, 395–403 (2014).
27. Binder, N. B. et al. Clinical use of thrombin generation assays. *J. Thromb. Haemost.* **19**, 2918–2929 (2021).
28. Macfarlane, R. G. & Biggs, R. A thrombin generation test; the application in haemophilia and thrombocytopenia. *J. Clin. Pathol.* **6**, 3–8 (1953).
29. Pitney, W. R. & Dacie, J. V. A simple method of studying the generation of thrombin in recalcified plasma; application in the investigation of haemophilia. *J. Clin. Pathol.* **6**, 9–14 (1953).
30. Hemker, H. C. et al. The calibrated automated thrombogram (CAT): a universal routine test for hyper- and hypocoagulability. *Pathophysiol. Haemost. Thromb.* **32**, 249–253 (2002).
31. Gerotziafas, G. T. et al. Comparison of the effect of fondaparinux and enoxaparin on thrombin generation during in-vitro clotting of whole blood and platelet-rich plasma. *Blood Coagul. Fibrinolysis* **15**, 149–156 (2004).
32. Zavyalova, E. & Kopylov, A. Exploring potential anticoagulant drug formulations using thrombin generation test. *Biochem. Biophys. Rep.* **5**, 111–119 (2016).
33. Wheeler, T. D. & Stroock, A. D. The transpiration of water at negative pressures in a synthetic tree. *Nature* **455**, 208–212 (2008).
34. Gokce, O., Castonguay, S., Temiz, Y., Gervais, T. & Delamarche, E. Self-coalescing flows in microfluidics for pulse-shaped delivery of reagents. *Nature* **574**, 228–232 (2019).

Article

Methods

Chip design and fabrication

The chips were designed using AutoCAD (Autodesk) and exported as .STL files for 3D printing. CCs encoding MCRs were made with a digital micromirror display (DMD) 3D printer (Miicraft 100, Creative Cadworks) using a transparent resin (Rapid Model Resin Clear, Monocure 3D) purchased from filaments.ca. The following printing parameters were used: the layer thickness was 20 μm and the exposure time 1.5 s per layer, whereas the exposure time for the base layer was 10 s with four transition buffer layers. Following completion of the print, the chips were cleaned with isopropanol and post-cured for 1 min under ultraviolet (UV) light (Professional CureZone, Creative Cadworks).

Microchannels with cross-sections ranging from 250×100 to $1,500 \times 1,000$ μm^2 were fabricated and hydrophilized by plasma activation for 10 s at approximately 30% power (PE50 plasma chamber, Plasma Etch).

CCs were sealed with a delayed tack adhesive tape (9795R microfluidic tape, 3M) forming the cover.

Paper capillary pump

Filter papers (Whatman filter paper grade 4, 1 and 50 Hardened, Cytiva) were used as paper capillary pumps for all experiments except the SARS-CoV-2 antibody assay. The pore size from 4, 1 and 50 hardened is in decreasing order, and flow resistance and capillary pressure increase with decreasing pore size.

For the SARS-CoV-2 antibody assay, absorbent pads (Electrophoresis and Blotting Paper, Grade 238, Ahlstrom-Munksjo Chromatography) were used as pumps.

Chip-to-chip connections for the 300 capillary flow events

To obtain a leakage-free connection, a thin layer of uncured photoresin, prepared by mixing poly (ethylene glycol) diacrylate (PEG-DA MW 258, Sigma-Aldrich) and Irgacure-819 (1% w/w), was applied to all of the chip-to-chip interfaces. Next, the chips were assembled and exposed to UV light in a UV chamber (320–390 nm, UVitron Intelliray 600) at 50% intensity for 30 s to cure the resin and seal the connections.

Videos and image processing

Videos and images were recorded using a Panasonic Lumix DMC-GH3K. Structural images of the chip and the embedded conduits were obtained using micro-computed tomography (Skyscan 1172, Bruker) and used to confirm the dimensions. Contact angles were measured on the basis of side view images ($n = 3$) and analysed using the Dropsnake extension in Image J.

Modelling and calculations

The theoretical burst pressures of capillary SVs were calculated by solving the flow field using the finite element method with COMSOL Multiphysics v.5.5. Experimentally measured contact angles (100° and 40° for the cover and the channel, respectively) were used to solve two-phase capillary flow using the level-set method. The capillary flows leading up to the SV was solved for a time period of 0–0.02 s with a time step of 1×10^{-5} s. The inlet pressure was varied with 10 Pa increment for each simulation until a burst was observed.

Experiments on pressure thresholds for capillary SV and RBV

We 3D-printed modules to evaluate SV/RBV with different cross-section areas. Each module contained three SV/RBV for replicate results. SV/RBV consisted of a two-level SV based on a geometrical channel expansion, as described elsewhere[12]. The chips integrated a conical inlet/outlet for tubing connection to a microfluidic flow controller system (MFCS-4C) and Fluiwell package (Fluigent) with fluidic reservoirs containing 5% red food dye in MilliQ water solution (see Extended Data Fig. 4 for setup images and Fig. 2 for contact angles). MAESFLO v.3.3.1 software (Fluigent) controlled the application of positive or negative pressure to calculate the burst pressures of the SV (liquid burst into air link) and RBV (receding meniscus), with increments of 0.1 mbar (roughly 10 Pa).

SARS-CoV-2 antibody assay

Reagents. SARS-CoV-2 nucleocapsid protein was purchased from Sino Biological, Inc. (40588-V08B). Human Chimeric antibody against SARS-CoV-2 nucleocapsid protein was purchased from Genscript Biotech (A02039). SIGMAFAST 3,3′-diaminobenzidine tablets were purchased from Sigma-Aldrich. Biotinylated Goat-anti-Human antibody was purchased from Cedarlane (GTXHU-003-DBIO). Pierce streptavidin poly-HRP (21140) was purchased from ThermoFisher.

Nitrocellulose strips. Nitrocellulose membranes (Whatman FF80HP Plus nitrocellulose-backed membranes, Cytiva) were cut into 5.2-mm-wide strips using the Silhouette Portrait paper cutter (Silhouette). Membranes were striped with a 5-mm-wide test line of 0.25 mg ml^{-1} SARS-CoV-2 nucleocapsid protein delivered using a programmable inkjet spotter (sciFLEXARRAYER SX, Scienion). The test line consists of four lanes of 50 droplets of about 350 pl printed 100 μm apart from each other. Eight passes of 25 droplets were used for each lane on even and odd positions to allow solution absorption in between passes. The membranes were then dried for 1 h at 37 °C before blocking by dipping into 1% BSA in 1× PBS solution until completely wet, then retrieved and left to dry for 1 h at 37 °C and then stored with desiccant at 4 °C until use the next day.

Connection of capillary pump and nitrocellulose chip to MCR chips. Nitrocellulose strips were mounted following standard lateral flow assay assembly protocols. The nitrocellulose strip was connected to a glass fibre conjugate pad (G041 SureWick, Millipore Sigma) on one end, and to an absorbent pad (Electrophoresis and Blotting Paper, Grade 238, Ahlstrom-Munksjo Chromatography) serving as the capillary pump at the other end. All three were attached to an adhesive tape serving as the backing layer. For the saliva antibody assay, the nitrocellulose strip was sandwiched between three absorbent pads (15×25 mm^2) and clamped with a paper clip. For the food-dye demonstrations a single absorbent pad (25×45 mm^2) was magnetically clamped to the nitrocellulose membrane.

Saliva assay protocol. Human saliva was extracted with oral swabs (SalivaBio, Salimetrics), followed by centrifugation and 1:10 dilution with 0.22 μM filtered phosphate buffer saline containing 1% BSA, 0.1% Tween 20. Human chimeric antibody against SARS-CoV-2 nucleocapsid protein at 0 to 1,000 ng ml^{-1} was spiked into diluted saliva and loaded to the sample reservoirs. Three replicate measurements for concentrations of 0–10 ng ml^{-1}, two replicate measurements for concentrations of 30–300 ng ml^{-1} and one measurement for 1,000 ng ml^{-1}. Biotinylated goat anti-human antibody at 0.5 μg ml^{-1} and streptavidin poly-HRP at 0.5 μg ml^{-1} were used to detect the human antibody. Control line in the nitrocellulose strip confirms reagents delivery and colorimetric reaction completion.

Image analysis on the nitrocellulose strips. After drainage of all reservoirs, the nitrocellulose membrane strip was removed, placed on a support and left to dry for 1 h.

The dry strips were imaged using (1) a flatbed scanner (mfc-9970cdw, Brother) at a resolution of 600 dpi and (2) using a Huawei P10 smartphone with a 12 megapixel image sensor and a rear camera with a 27 mm focal length (Huawei) in a customized box. The box was cut and folded with black cardboard paper to block ambient light when imaging with the smartphone. The box had two slots fitting the size of camera and nitrocellulose strip, respectively, to ensure accurate alignment of the strip for readout. Images were taken with on-camera dual tone

light-emitting diode flash at full power. Analysis of smartphone-taken and scanned images was done as follows.

Mean grey values of nitrocellulose test lines were extracted with ImageJ 1.48v (ImageJ, public domain software, W. Rasband, National Institutes of Health) within a 100×10 pixel rectangular area. Local background grey values were taken at 2.5 mm (0.1 inch) above each test line (following direction of the flow) for the same rectangular area, and subtracted from test line values. The normalized standard curve was then generated by subtracting negative control signal value (0 ng ml^{-1}) from all data points.

The limit of detection was calculated using the three-sigma criterion using a non-linear four-parameter logistic curve fit of the log-transformed data with OriginPro 8.5 SPR (OriginLab Corporation).

Automated microfluidic TGA (Thrombochip). Citrated human plasma (P9523, lot number SLBX8880), fluorogenic thrombin substrate Z-GGR-AMC and Enoxaparin were purchased from Sigma-Aldrich; Batroxobin was from Prospec; Technothrombin TGA RC High reagent was from Diapharma; Human thrombin, non-patient plasma that were immuno-depleted of Factor V and Factor IX, and Factor VIII inactivated were from Haematologic Technologies; (4-(2-hydroxyethyl)-1-piperazineethanesulfonic acid) (HEPES), and ethylenediaminetetraacetic acid (EDTA) and CaCl$_2$ were from Sigma-Aldrich.

The purchased pooled human plasma (collected in the United States in a Food and Drug Administration licensed centre site no. 268, as specified in the Certificate of Origin supplied by the manufacturer) was prepared by the manufacturer from whole blood collected by standard industry method using 4% trisodium citrate as an anticoagulant, pooled and then centrifuged. The resulting plasma was 0.45 µm filtered and lyophilized. Factor V- and Factor IX-depleted plasma were immune depleted; Factor VIII-depleted plasma was prepared by chemical depletion. The plasma preparations were assayed to ensure the activity of the remaining factors by the manufacturer.

Human plasma (pooled normal or factor depleted) were defibrinated by the addition of batroxobin (final concentration 0.6 BU ml^{-1}). The mixtures were incubated at room temperature for 20 min, followed by an extra incubation at 4 °C for 1 h. The mixtures were then centrifuged at 10,000g for 10 min to remove the fibrin clot and other debris. Defibrinated plasma were collected from the supernatant.

A solution containing 21% defibrinated plasma (plasma defibrination is needed to prevent clogging of the microfluidic channels by the fibrin clot), 48% Technothrombin TGA RC High reagent (high phospholipid and relipidated tissue factor content) and 20 mM CaCl$_2$ in 25 mM HEPES at pH 7.4 was loaded into the sample reservoirs of the thrombochip. A substrate solution containing 420 µM Z-GGR-AMC, 30 mM EDTA in 25 mM HEPES at pH 7.4 was loaded into the reagent reservoirs. The concentration of plasma, activation agent and substrate were optimized to yield a peak thrombin concentration and time of 150 nM and 200 s. All solutions were equilibrated to room temperature for 20 min before loading. Coagulation-inhibited plasma contained Enoxaparin at final concentrations of 0 to 1.0 anti-Xa units ml^{-1} or IU ml^{-1}. The samples and reagents were loaded on the chip after initiating the coagulation cascade. The paper pump was connected to the chip to start the flow after 5 min from initiating the coagulation cascade. Fluorescence signals generated in the reaction chambers were monitored by illuminating the thrombochip with UV light at 365 nm with 20 W (realUV LED Flood Light, Waveform Lighting) and the visible 440 nm fluorescence

emission signals measured by imaging at 5 s intervals using a Panasonic Lumix DMC-GH3K digital camera (f/3.5, Exposure time: 2 s, ISO-200). The rate of fluorescence signal generation in each reaction chamber (that is, the slope of the recorded fluorescence generation curve) is a measure of the rate of substrate turnover by thrombin and was used to deduce the amount of thrombin generated using a standard curve. ImageJ was used to analyse the images for fluorescence intensity.

Standard curve for thrombin quantification. Ten human thrombin solutions at concentrations ranging from 0 to 300 nM in 25 mM HEPES at pH 7.4 were loaded into the ten sample reservoirs in the thrombochip. A substrate solution containing 420 µM Z-GGR-AMC, 30 mM EDTA in 25 mM HEPES at pH 7.4 was loaded into the reagent reservoirs. The standard curve was constructed by plotting the slope of the recorded fluorescence generation curve in each reaction chamber against the known thrombin concentration of the solution that was loaded to the corresponding sample reservoir.

Reporting summary

Further information on research design is available in the Nature Research Reporting Summary linked to this paper.

Data availability

The 3D design files of the MCR-CC chips are included as part of this article, and are also available for download along with more images and descriptions at https://www.thingiverse.com/junckerlab/collections/microfluidic-chain-reaction-of-structurally-programmed-capillary-flow-events. Data not presented in the article or supplementary material will be available upon request. Source data are provided with this paper.
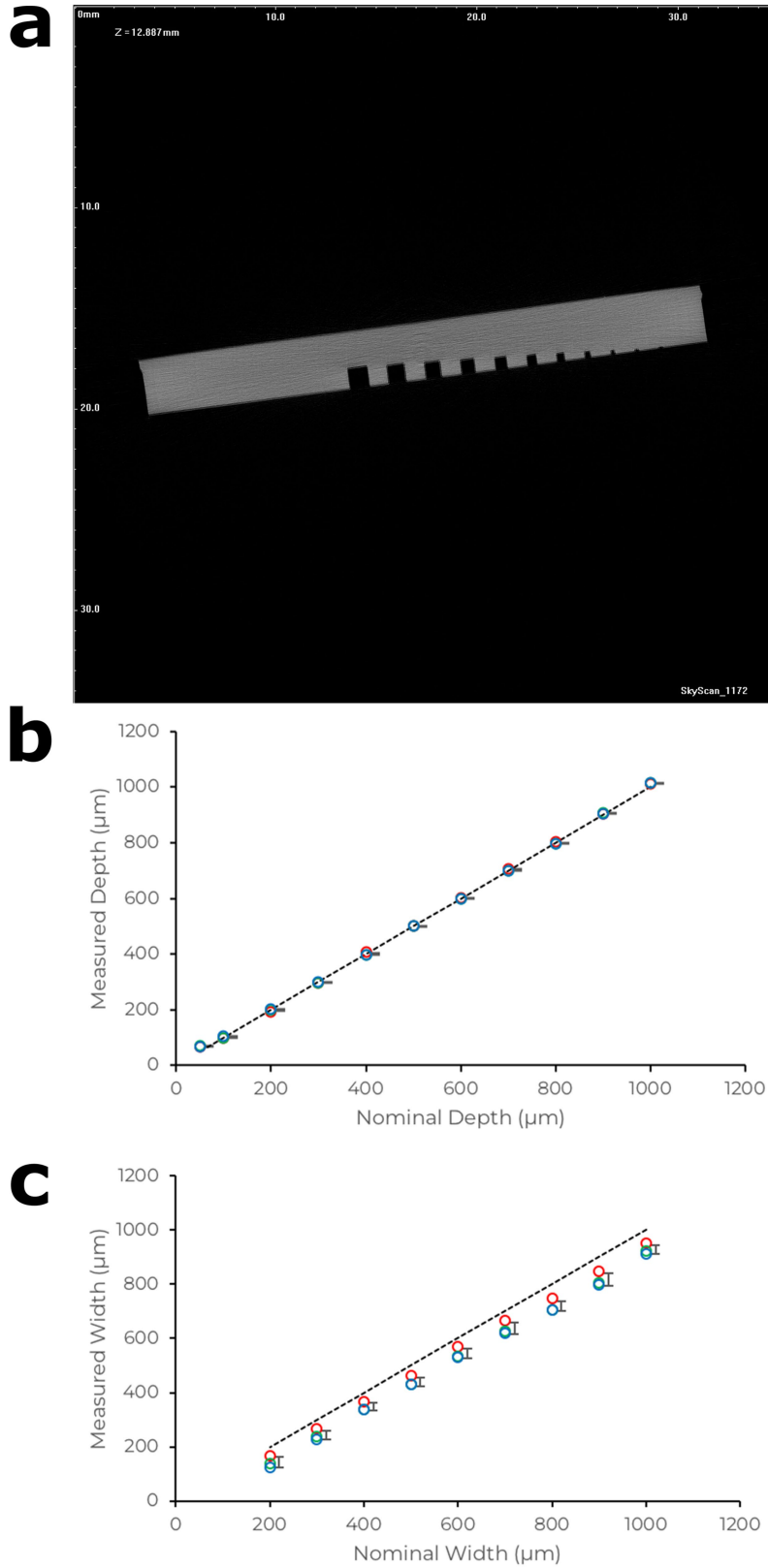
Extended Data Fig. 1 | Designed and measured dimensions of 3D-printed channels. (**a**) CT scan channels with square cross-section with different width and depth. (**b**) Measured depth of 3D-printed channels matches the nominal, designed depth. (**c**) The measured width of 3D-printed channels is ~40 µm smaller than the designed width. Dashed line shows the 1:1 ratio. All data points are shown. Error bars (presented on the right side of the data points for clarity) are standard deviation of the measurement of 3 replicate channels; the centre of each error bar is the mean measurement value.

a

b
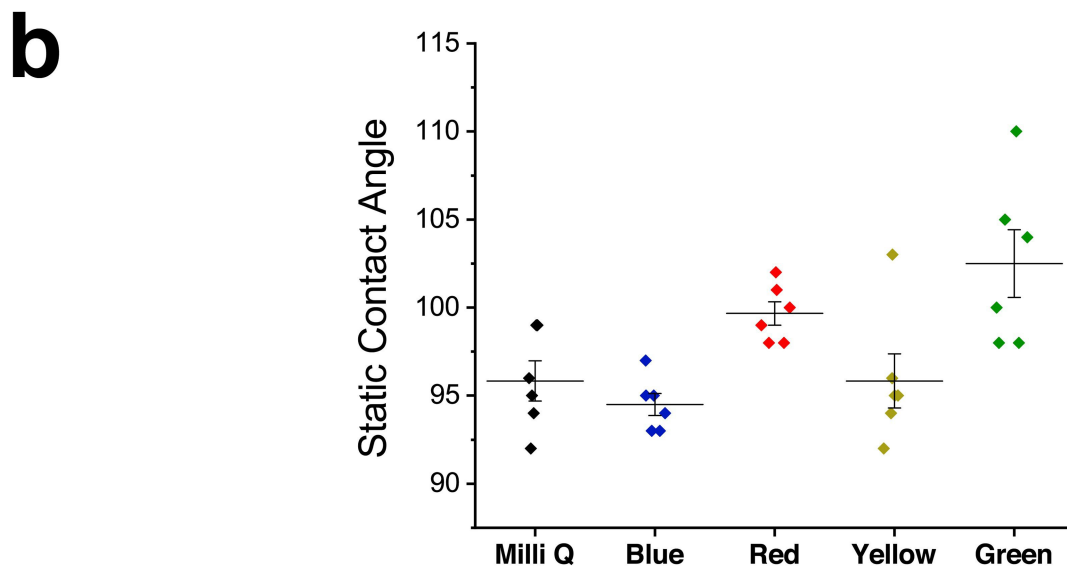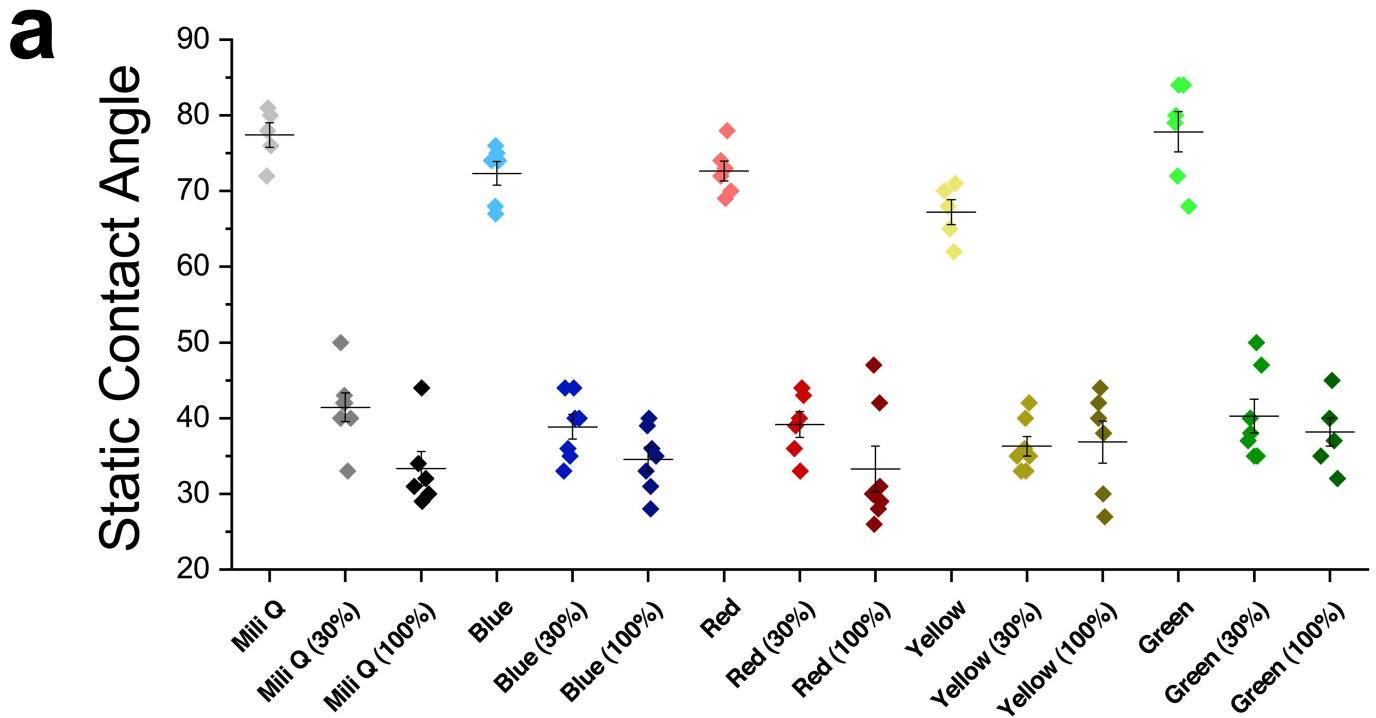
Extended Data Fig. 2 | Contact angles of water without and with food dyes on materials used for MCR CC. (**a**) Contact angle of Milli Q water and different food dyes used in the experiments on the 3D-printed resin used for making the MCR CCs that were pristine (without plasma treatment) and following plasma treatment for 10 s at 30% and 100% plasma power. (**b**) Contact angle on the hydrophobic tape (3M microfluidic tape 9795R) used as cover. All data points are shown. Error bars are standard deviation of 6 replicate measurements; the centre of each error bar is the mean value.
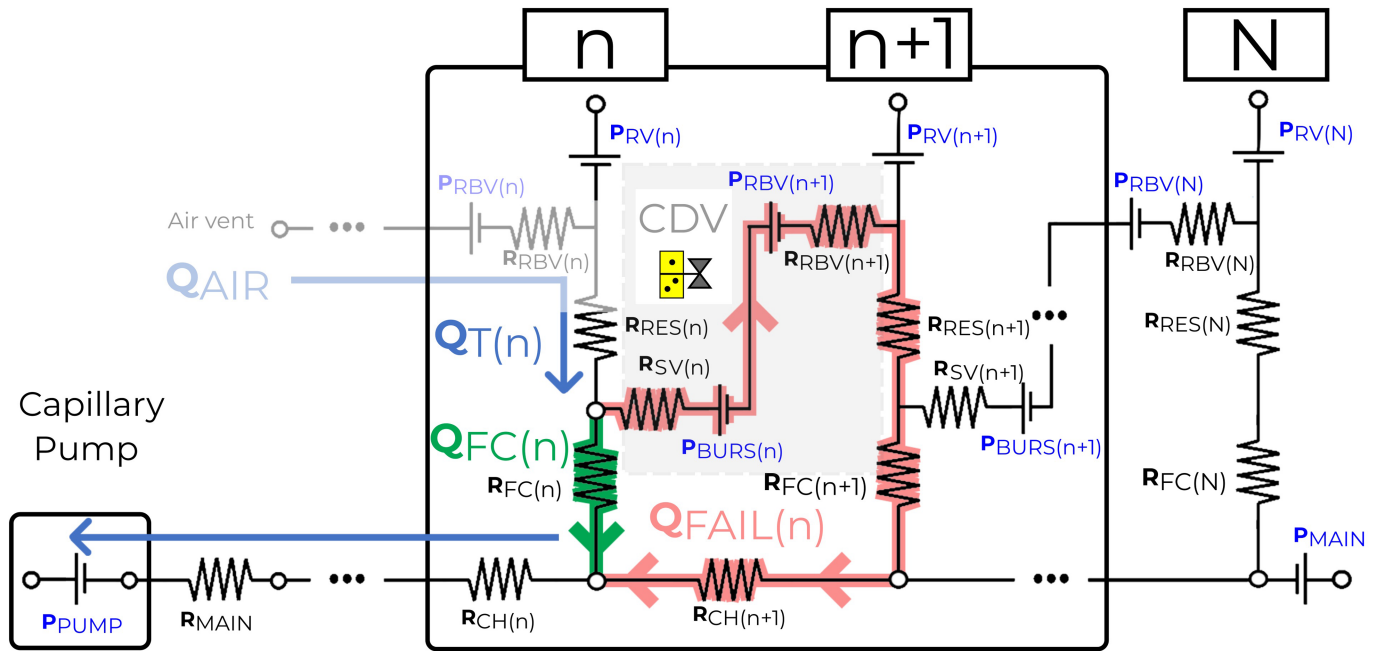
Extended Data Fig. 3 | Equivalent resistance and pressure source diagram for an MCR unit including capillary domino valve (CDV) and functional connection (FC). The pressure drop $P_{FC} = Q_{T(n)} \times R_{FC}$ with $Q_{T(n)}$ the total flow rate which is equal to Q_{FC} if all the flow flows through the functional connection, and also equal to Q_{Air} drawn in to replace the liquid drained from the reservoir, and is the condition for successful operation. The overall resistance of the main channel and capillary pump is R_{MAIN}. In our designs, the resistances for the reservoir R_{RES}, the stop valve R_{SV}, the retention burst valve R_{RBV} and the sections of the main channel $R_{CH(n)}$ are much smaller than R_{MAIN} and R_{FC}, and hence can be neglected when calculating $Q_{T(n)} \approx P_{PUMP}/(R_{MAIN} + R_{FC})$ and are also negligible for the CDV failure analysis and ignored in the simplified schematic of Fig. 2a. The capillary retention valve threshold pressure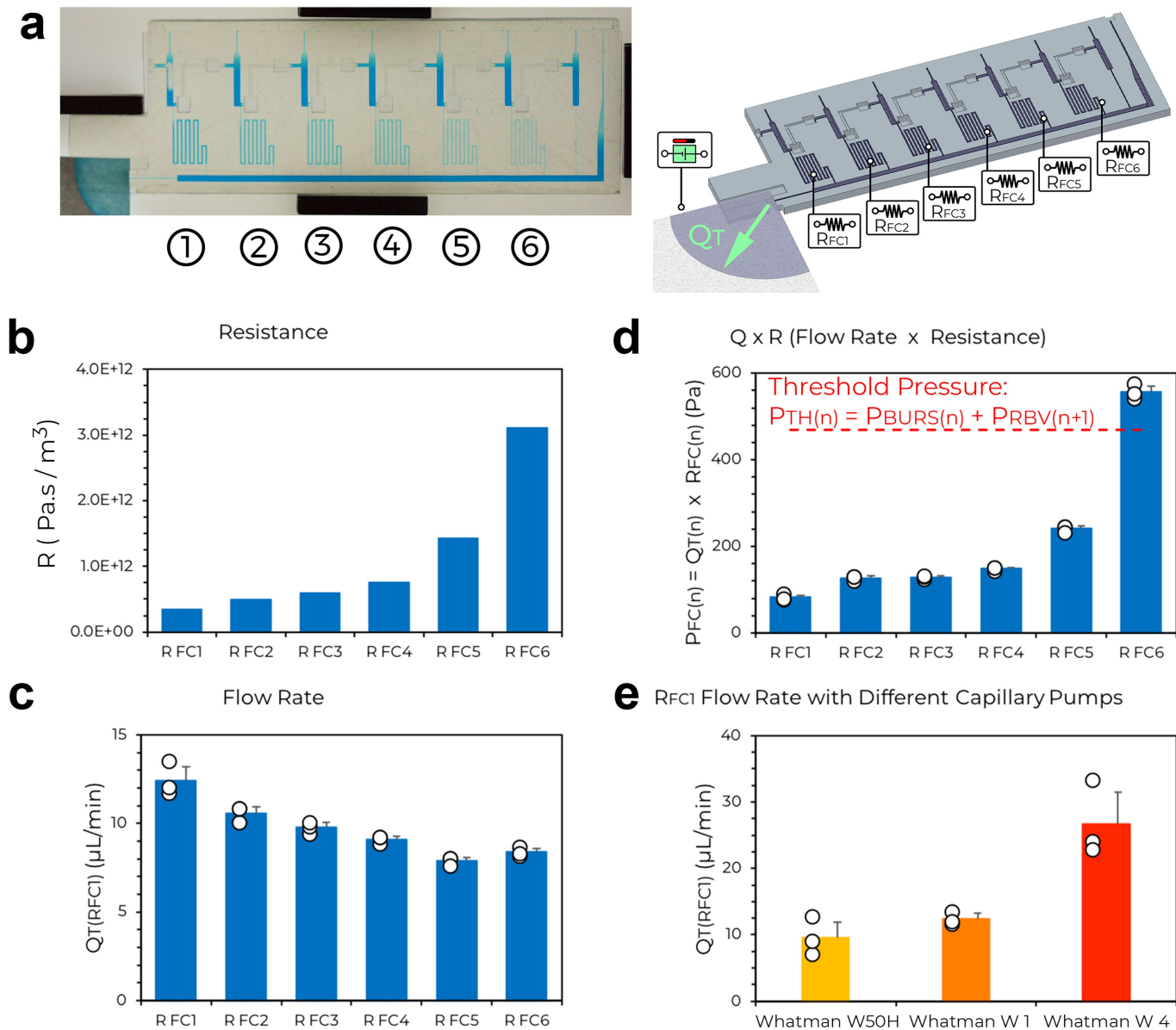 is indicated as P_{RV} for side channels and P_{MAIN} for the main channel, and their pressure will match the one in the liquid (relative to air) up the bursting threshold of the valve and are designed such that they do not burst. The retention burst valve pressure is P_{RBV} and the stop valve pressure is P_{BURS} and both will adopt the pressure value difference between the air link and the adjacent liquid, up to their bursting threshold. Failure of either means failure of the other as they are pneumatically linked (until reservoir n is emptied, and the condition for chain reaction propagation is met, that is), and also failure of the CDV and the MCR because liquid will penetrate into the CDV and the air link, and clog it, which is indicated by Q_{FAIL}. Hence the condition for successful operation and propagation of the MCR to the final reservoir N is $Q_{FAIL} = 0$ for each of the chain reaction steps.
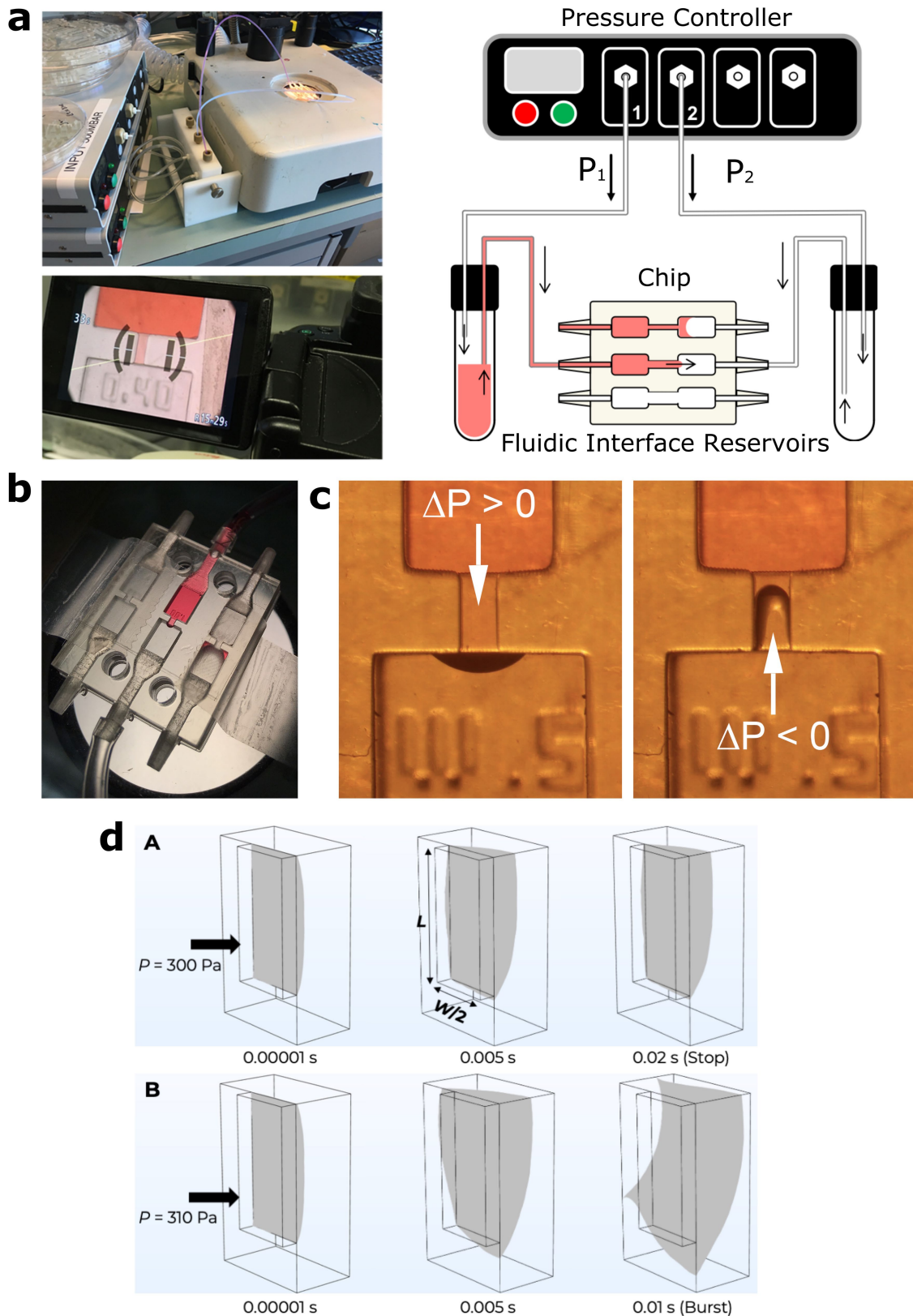
Extended Data Fig. 4 | SV/RBV burst pressure experiments and simulation. (**a**) Experimental setup for the positive and negative burst pressure experiments for the stop valve (SV) and retention burst valve (RBV) respectively. We connected a microfluidic flow controller system to the 3D-printed microfluidic chip containing three geometric two-level stop valves, and different chips were fabricated with varied cross-section valves dimensions. We used a camera to record videos to evaluate the valve burst pressure tested with increments of 0.1 mbar (~10 Pa). (**b**) Close-up picture of a chip with the middle valve under evaluation. (**c**) Valve positive (left) and negative (right) burst pressure experiments. (**d**) Screenshots of the burst pressure by finite element method simulation for the stop valve showing successful stop at 300 Pa, and bursting for 310 Pa.

a

b Resistance

c Flow Rate

d Q x R (Flow Rate x Resistance)

Threshold Pressure:
$P_{TH(n)} = P_{BURS(n)} + P_{RBV(n+1)}$

e R_{FC1} Flow Rate with Different Capillary Pumps

Extended Data Fig. 5 | Experimental operating window for CDV and MCR.
(**a**) Test chip for evaluating determining the operational window of the CDV and breach. The chip includes 6 functional connections with serpentines with constant width and decreasing channel depth of 500, 300, 240, 200, 140, and 100 μm, respectively, and hence increasing R_{FC}. The rightmost reservoir is needed to test the functional connection no. 6. (**b**) R_{FC} for each of the design variations (R_{FC1} to R_{FC6}) (see also Fig. 2d). (**c**) The flow rate for each reservoir with a medium rate paper pump (Whatman filter paper 1). (**d**) With Whatman paper 1

pump, bursting of liquid into the CDV and air link was only observed for the last reservoir. (**e**) flow rate measurements for R_{FC1} for the three different Whatman paper pumps with grade 4, 1 and hardened 50. All data points are shown in (**c**–**e**). Error bars are standard deviation of 3 replicate measurements, the centre of each error bar is the mean value. The capillary pump with the lowest flow resistance resulted in the highest flow rate. The CDV failure occurred when the pressure drop across the functional connection exceeds the threshold pressure (Fig. 2a).

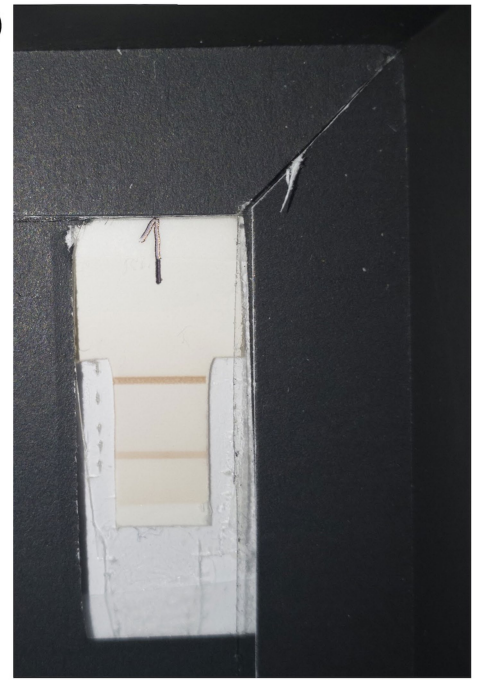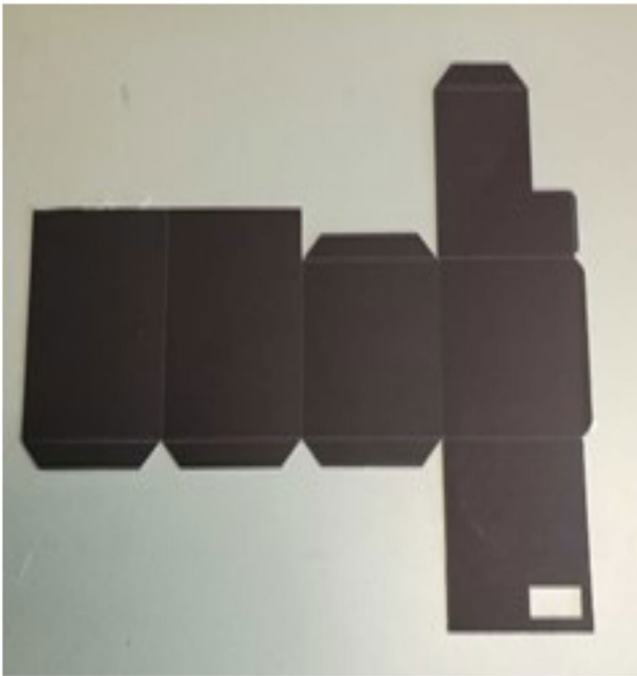**a** Negative Control (0 ng/mL) Test Line Signal Optimisation
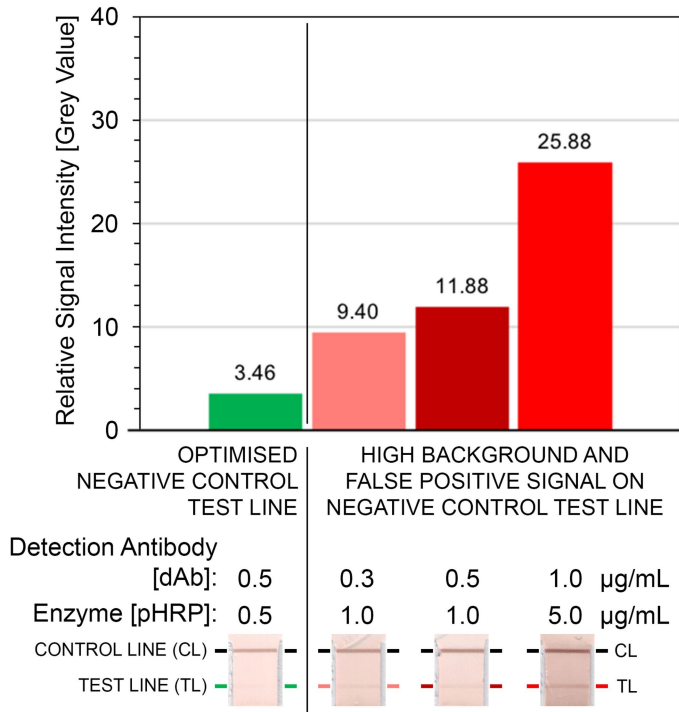
b Assay Standard Curve Signal Optimisation
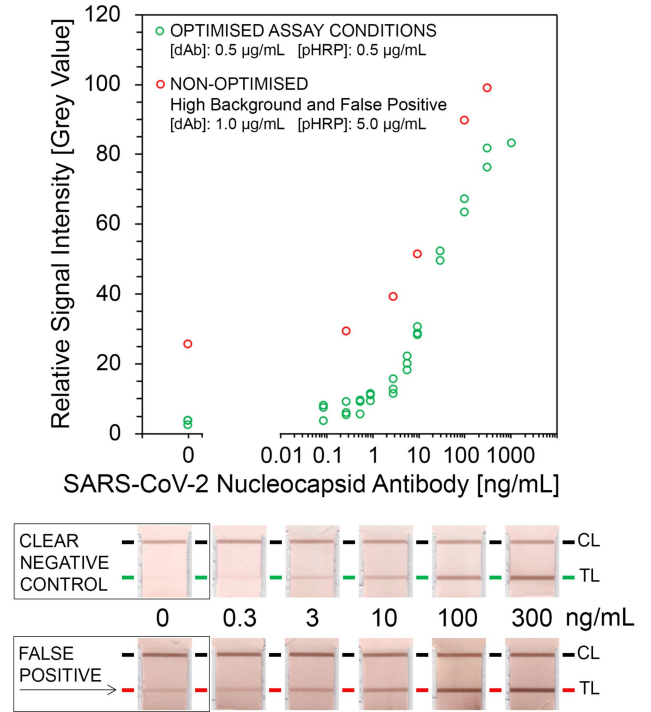
Extended Data Fig. 6 | SARS-CoV-2 antibody assay optimization examples. (a) Reduction of background signal. The graph and nitrocellulose strips (below) show the grey value of the test line (TL) after running four chips with different reagent 3 (see Fig. 3b; biotinylated goat-anti-human antibody used as detection antibody) and reagent 5 (streptavidin-Poly-HRP as enzyme)

concentrations. (b) Assay performance using non-optimized (red) and optimized concentrations of reagents 3 and 5 (green). Non-optimized conditions show high background and false positive signal on the test line for the negative control membrane strip.

a
SCANNER

b
SMARTPHONE

0 ng/mL

0.1 ng/mL

0.3 ng/mL

0.6 ng/mL

1.0 ng/mL

3.0 ng/mL

6.0 ng/mL

10 ng/mL

30 ng/mL

100 ng/mL

300 ng/mL

1000 ng/mL

Extended Data Fig. 7 | SARS-CoV-2 antibody assay on nitrocellulose membranes. Array of the nitrocellulose membrane strips images of the optimized conditions for the detection of SARS-CoV-2 nucleocapsid antibody in saliva at different concentrations, presented in Fig. 3c. On the left (**a**) pictures taken by a scanner (highlighted green test line) and right (**b**) by a smartphone camera (orange test line).

Extended Data Fig. 8 | Foldable box for reducing light interference during smartphone-based test readout. (**a**) Smartphone and folded cardboard setup used to measure the signal of the SARS-CoV-2 antibody assay. (**b**) Detail of smartphone picture taken using the foldable box. (**c**) Unfolded black box casing showing opening for smartphone camera lens and flash. (**d**) Assembled black box casing designed for images taken using smartphone with the built-in flash to analyze the signal line on the nitrocellulose membrane.
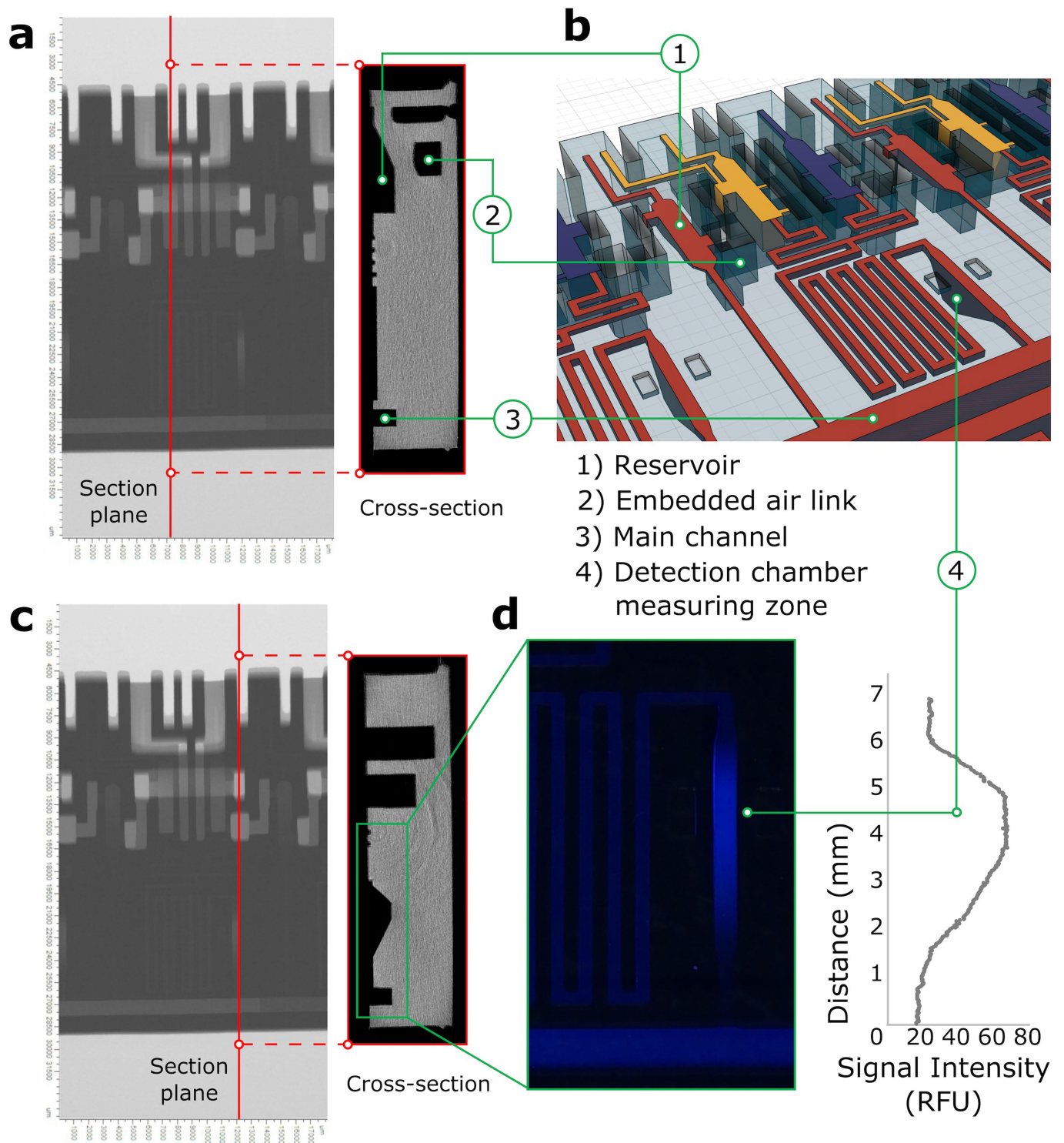
Extended Data Fig. 9 | Micro computer tomography images of 3D printed thrombochip. (**a**) micro CT scan at the cross-section of the reservoir and the embedded air link. (**b**) 3D schematic for one stage in the thrombochip design. (**c**) micro CT scan at the cross-section of the reaction chamber showing. (**d**) The fluorescence signal generated along the reaction chamber. The signal is measured at the deepest section, depicted as the measuring zone, to get the highest possible signal.

nature portfolio

Corresponding author(s): David Juncker

Last updated by author(s): Feb 14 2022

Reporting Summary

Nature Portfolio wishes to improve the reproducibility of the work that we publish. This form provides structure for consistency and transparency in reporting. For further information on Nature Portfolio policies, see our Editorial Policies and the Editorial Policy Checklist.

Statistics

For all statistical analyses, confirm that the following items are present in the figure legend, table legend, main text, or Methods section.

n/a	Confirmed	
☐	☒	The exact sample size (*n*) for each experimental group/condition, given as a discrete number and unit of measurement
☐	☒	A statement on whether measurements were taken from distinct samples or whether the same sample was measured repeatedly
☒	☐	The statistical test(s) used AND whether they are one- or two-sided *Only common tests should be described solely by name; describe more complex techniques in the Methods section.*
☒	☐	A description of all covariates tested
☒	☐	A description of any assumptions or corrections, such as tests of normality and adjustment for multiple comparisons
☐	☒	A full description of the statistical parameters including central tendency (e.g. means) or other basic estimates (e.g. regression coefficient) AND variation (e.g. standard deviation) or associated estimates of uncertainty (e.g. confidence intervals)
☒	☐	For null hypothesis testing, the test statistic (e.g. *F*, *t*, *r*) with confidence intervals, effect sizes, degrees of freedom and *P* value noted *Give P values as exact values whenever suitable.*
☒	☐	For Bayesian analysis, information on the choice of priors and Markov chain Monte Carlo settings
☒	☐	For hierarchical and complex designs, identification of the appropriate level for tests and full reporting of outcomes
☒	☐	Estimates of effect sizes (e.g. Cohen's *d*, Pearson's *r*), indicating how they were calculated

Our web collection on statistics for biologists contains articles on many of the points above.

Software and code

Policy information about availability of computer code

Data collection	Micro CT Images acquired with Bruker data viewer; COVID19 serology with scanner and cell phone; Thrombogram with Panasonics G3
Data analysis	Graphpad Prism 9, Microsoft Excel v16, COMSOL Multiphysics 5.5, MAESFLO 3.3.1, Image J 1.48v, OriginPro 8.5 SPR, Micro CT Image analysis with Bruker CTAN

For manuscripts utilizing custom algorithms or software that are central to the research but not yet described in published literature, software must be made available to editors and reviewers. We strongly encourage code deposition in a community repository (e.g. GitHub). See the Nature Portfolio guidelines for submitting code & software for further information.

Data

Policy information about availability of data

All manuscripts must include a data availability statement. This statement should provide the following information, where applicable:

- Accession codes, unique identifiers, or web links for publicly available datasets
- A description of any restrictions on data availability
- For clinical datasets or third party data, please ensure that the statement adheres to our policy

3D design files of the MCR-CC chips are included as part of this article, and are available for download along with additional images and descriptions at https://www.thingiverse.com/junckerlab/collections/microfluidic-chain-reaction-of-structurally-programmed-capillary-flow-events. All raw and processed data available upon request.

Field-specific reporting

Please select the one below that is the best fit for your research. If you are not sure, read the appropriate sections before making your selection.

☒ Life sciences   ☐ Behavioural & social sciences   ☐ Ecological, evolutionary & environmental sciences

For a reference copy of the document with all sections, see nature.com/documents/nr-reporting-summary-flat.pdf

Life sciences study design

All studies must disclose on these points even when the disclosure is negative.

Sample size	In the COVID-19 serology experiment, the mean value from three spike-in replicates, along with the standard deviation value of the negative control were used to generate a standard curve and the limit of detection. In the thrombochip experiment, no statistical analysis was performed. Replicate measurement were aimed to demonstrate reproducibility of the assay and were performed using a single sample.
Data exclusions	Experiments where the microfluidic operations were clearly not running properly, or failed, due to fabrication and assembly issues and errors were discarded.
Replication	In the COVID-19 serology experiment, 3 replicates were measured using a single sample spiked with the analyte for concentrations 0-10 ng/mL; 2 replicate measurements for concentrations 30-300 ng/mL, and one measurement for 1,000 ng/mL. In the thrombochip experiments, 3 replicates were performed with the same normal plasma sample, a single measurement was performed for each of the factor-deficient plasma, and a single measurement per drug concentration in the drug spike-in experiment. All attempts at replication were successful when the fluidic functions of the chips were successful.
Randomization	There were no requirement for randomization in our study since a single spike-in sample was used for replicate experiments. The experiments aimed to demonstrate the reproducibility of the assays (COVID-19 serology and thrombochip) and were not for generate biological findings.
Blinding	The nature of all samples were known to the investigators. Group allocation was not necessary in our study. Blinding during data collection was not required in this work as all assays were automatic, and raw data were measured through image analysis by software.

Reporting for specific materials, systems and methods

We require information from authors about some types of materials, experimental systems and methods used in many studies. Here, indicate whether each material, system or method listed is relevant to your study. If you are not sure if a list item applies to your research, read the appropriate section before selecting a response.

Materials & experimental systems

n/a	Involved in the study
☐	☒ Antibodies
☒	☐ Eukaryotic cell lines
☒	☐ Palaeontology and archaeology
☒	☐ Animals and other organisms
☐	☒ Human research participants
☒	☐ Clinical data
☒	☐ Dual use research of concern

Methods

n/a	Involved in the study
☒	☐ ChIP-seq
☒	☐ Flow cytometry
☒	☐ MRI-based neuroimaging

Antibodies

Antibodies used	Biotinylated Goat anti-Human IgG was purchased from Cedarlane, Burlington, Canada. Cat#: GaH-bt GtxHu-003-DBIO, Lot#: 65-189-080219. The antibody was diluted to 1 mg/mL as stock, and used at concentrations between 0.5 µg/mL to 50 µg/mL. Human Chimeric antibody against SARS-CoV-2 nucleocapsid protein was purchased from Genscript Biotech, Piscataway, USA. Cat #: A02039. Lot#: 20D002122. The antibody was diluted to 1 mg/mL as stock, and used in this study at concentrations between 0.5 ng/mL to 50 µg/mL.
Validation	Goat anti-Human IgG, Biotin Conjugate, Cat#: GaH-bt GtxHu-003-DBIO, have been validated by ImmunoReagents Inc., Validation data can be found through this link: https://www.immunoreagents.com/files/spec_sheets/1508051898_484-Goatanti-HumanIgGHL-AffinityPure-lot1.pdf SARS-CoV-2 Nucleocapsid Antibody (HC2003), Human Chimeric is produced from cell culture in vitro under conditions free from animal-derived components. Isotype: Recombinant human IgG1 Clone: HC2003 (monoclonal antibody) Purification: Protein A. They have been validated by Genscript. More details are available at this link https://www.genscript.com/antibody/A02039-SARS_CoV_2_Nucleocapsid_Antibody_HC2003_Human_Chimeric.html

Human research participants

Policy information about studies involving human research participants

Population characteristics	*Describe the covariate-relevant population characteristics of the human research participants (e.g. age, gender, genotypic information, past and current diagnosis and treatment categories). If you filled out the behavioural & social sciences study design questions and have nothing to add here, write "See above."*
Recruitment	*Describe how participants were recruited. Outline any potential self-selection bias or other biases that may be present and how these are likely to impact results.*
Ethics oversight	The purchased human pooled plasma (P9523, lot number SLBX8880, Sigma-Aldrich, Oakville, Canada) were collected in the USA in FDA licensed centre site #268, as specified in the Certificate of Origin supplied by the manufacturer.

Note that full information on the approval of the study protocol must also be provided in the manuscript.